arXiv:1612.01118v1 [cond-mat.mes-hall] 4 Dec 2016

Quantum transport through MoS_2 constrictions defined by photodoping

Alexander Epping,[†,‡,¶] Luca Banszerus,[‡,†,¶] Johannes Güttinger,[¶,‡] Luisa Krückeberg,[‡] Kenji Watanabe,[§] Takashi Taniguchi,[§] Fabian Hassler,[∥] Bernd Beschoten,[‡] and Christoph Stampfer[*,‡,¶]

These authors contributed equally to this work, JARA-FIT and 2nd Institute of Physics, RWTH Aachen University, 52074 Aachen, Germany, Peter Grünberg Institute (PGI-9), Forschungszentrum Jülich, 52425 Jülich, Germany, National Institute for Materials Science, 1-1 Namiki, Tsukuba, 305-0044, Japan , and JARA-Institute for Quantum Information, RWTH Aachen University, 52074 Aachen, Germany

Received December 6, 2016; E-mail: stampfer@physik.rwth-aachen.de

Abstract: We present a device scheme to explore mesoscopic transport through molybdenum disulfide (MoS_2) constrictions using photodoping. The devices are based on van-der-Waals heterostructures where few-layer MoS_2 flakes are partially encapsulated by hexagonal boron nitride (hBN) and covered by a few-layer graphene flake to fabricate several electrical contacts. Since the as-fabricated devices are insulating at low temperatures, we use photo-induced remote doping in the hBN to create free charge carriers in the MoS_2 layer. On top of the device, we place additional metal structures, which define the shape of the constriction and act as shadow masks during photodoping of the underlying MoS_2. Low temperature two- and four-terminal measurements show signatures of quantized conductance through these constrictions. The conductance steps have a height of e^2/h indicating the breaking of both valley and Kramers' degeneracy.

Van-der-Waals heterostructures based on graphene and transition metal dichalcogenides (TMDCs) are attracting increasing attention in mesoscopic physics and solid-state research.[1–6] One of the main challenges in this field is to find ways of confining carriers in well defined nanostructures. Achieving a high degree of control over carrier confinement is necessary for manipulating individual charges or spins,[7–10] as well as for investigating mesoscopic physics phenomena such as quantized conductance or valley filtering in bilayer graphene and TMDCs.[11] Moreover, good control over carrier confinement is a necessary requirement for studying fundamental material properties such as the g-factor and the charge carriers effective mass in mesoscopic devices.

Because of the absence of a band gap, mesoscopic physics in graphene is mostly studied in devices where the material has been etched into the desired shape.[5,6] These devices typically suffer from scattering and trap states on their rough edges.[6,12,13] In contrast, bilayer graphene[14,15] and semiconducting TMDCs[16,17] allow for smooth electrostatic confinement with the help of metallic gates, similarly to what has been pioneered in two-dimensional electron gases (2DEGs) in conventional semiconductor heterostructures for the past decades.[8,18,19]

Here, we demonstrate a new method of obtaining confinement in van-der-Waals heterostructures based on few-layers MoS_2 encapsulated in hexagonal boron nitride (hBN). In analogy to remote doping in semiconductor 2DEGs, we make use of the photodoping effect recently observed in hBN-graphene heterostructures.[20,21] We use this effect to define stable and smooth sub-wavelength lateral doping profiles in MoS_2 employing metal shadow masks that are lithographically defined on top of an hBN/MoS_2/hBN heterostructure. Our photo-induced remote doping approach enables us to reach free charge carrier densities of up to 10^{13} cm^{-2}, when using an additional gate voltage during light illumination. It thus allows to create arbitrary carrier density profiles defined by the shadow mask geometry. The feasibility of our approach is demonstrated by studying quantum transport through constrictions in MoS_2. We expect that our method allows to fabricate more complex doping geometries such as antidot lattices or Aharonov-Bohm rings with the advantage that the metal used for shadow masking does not need to be electrically contacted, when studying mesoscopic transport.

All samples are fabricated using the well-established dry van-der-Waals stacking technique,[22,23] but we employ only a single transfer step to fabricate all few-layer graphene contacts. A few-layer MoS_2 crystal gets partially encapsulated between two hBN flakes and is then placed onto a Si^{++}/SiO_2 substrate (Figure 1a). In order to electrically contact the MoS_2 from the top surface, the left and the right parts of the MoS_2 flake remain uncovered by the upper hBN crystal. At the same time, the inner fully encapsulated area of MoS_2 is well protected against transfer related degradation and contamination ensuring a high quality of the device. Thereafter, one large flake of few-layer graphene (FLG) is placed on top of the entire structure, which is in direct contact with MoS_2 in all parts that are not protected by the upper hBN flake (Figure 1b). Figure 1d shows an optical microscopy image of such a complete van-der-Waals stack. In contrast to previous reports,[24–26] where multiple flakes of FLG have been transferred to fabricate electrical contacts, we only transfer a single large FLG flake that is subsequently patterned (Figure 1c). Using a single flake to contact multi-terminal MoS_2 devices is convenient, as it saves several transfer steps or crystal phase engineering of the MoS_2.[27] Furthermore, it prevents any direct contact of solvents or wet chemistry with the MoS_2. When immersed in solvents, even the outer parts of the MoS_2 are fully encapsulated by the FLG. Electron-beam lithography and reactive ion etching (RIE) using an Ar/O_2 plasma allow to selectively etch the FLG and the MoS_2, while the etching rate is negligible for the top hBN. The graphene above the top hBN and several trenches through the MoS_2 are etched. The trenches are needed to separate the individual leads on each side of the multi-terminal devices (see illustration in Figure 1g). In a last step, Ti/Au contacts to the FLG, as well as the shadow mask structures for the constriction on the top hBN (see also Figure 1c) are evaporated, followed by lift-off.

The devices are characterized by scanning confocal Raman microscopy which enables us to spatially probe the structural (and partly electronic) quality of all individual layers of the van-der-

[†]These authors contributed equally to this work

[‡]JARA-FIT and 2nd Institute of Physics, RWTH Aachen University, 52074 Aachen, Germany

[¶]Peter Grünberg Institute (PGI-9), Forschungszentrum Jülich, 52425 Jülich, Germany

[§]National Institute for Materials Science, 1-1 Namiki, Tsukuba, 305-0044, Japan

[∥]JARA-Institute for Quantum Information, RWTH Aachen University, 52074 Aachen, Germany

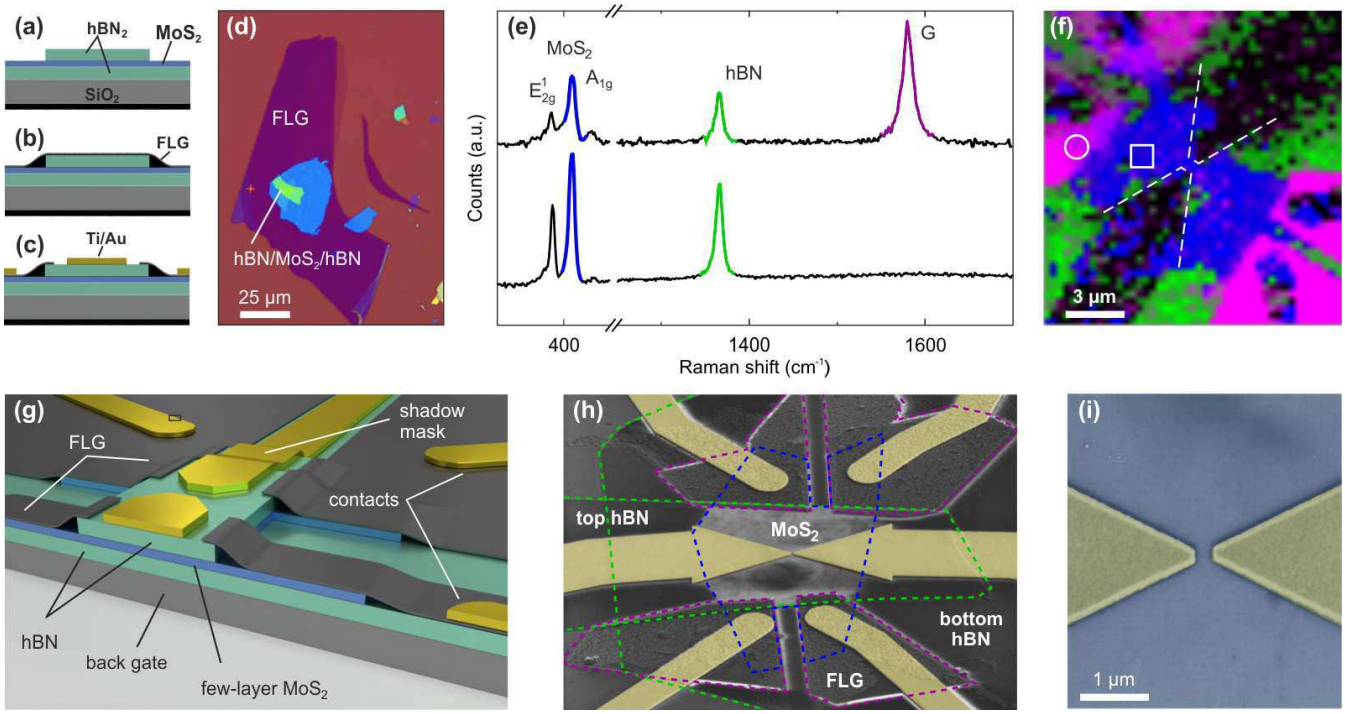

Figure 1. (a)-(c) Schematic illustration of the device fabrication. (a) MoS_2 is partially encapsulated by two hBN flakes. (b) A few-layer graphene flake is transferred over the entire heterostructure. (c) After etching the graphene into the desired shape, the shadow mask structure and the contacts are made. (d) Optical microscope image of the complete van-der-Waals heterostructure. (e) Raman spectra on a final device recorded in the lead area indicated by the white circle in panel (f) (top) and in the sandwiched part of the device indicated by the white square in panel (f) (bottom) showing the individual Raman peaks of hBN (green), graphene (purple) and MoS_2 (blue). (f) Raman map showing the integrated intensities of the hBN peak, the G-peak of the FLG and the A_{1g} mode of the MoS_2, represented by the colors purple, blue and green, respectively. The black areas are covered by metal whose boundaries are indicated by the white dashed lines. (g) Schematic of a typical multi-terminal device. (h) Scanning electron microscopy image of a four-terminal device. The individual flakes are highlighted by dashed lines with the same color as in panel (e). (i) Close-up of the shadow mask that forms a 250 nm wide constriction.

Waals heterostructure. Figure 1e depicts two typical Raman spectra. The upper spectrum in Figure 1e is recorded in the lead area (see open circle in Figure 1f), where the MoS_2 is covered with FLG. The G-peak at 1583 cm^{-1} (purple) originates from the FLG.[28] The hBN peak is located at around 1365 cm^{-1} (green)[29] while the A_{1g} and the E^1_{2g} modes of the MoS_2 are located at 409 cm^{-1} (blue) and 386 cm^{-1}, respectively.[30,31] The lower spectrum in Figure 1e is recorded on the hBN/MoS_2/hBN area of the device, close to the shadow masks, where only the two peaks from the hBN and the MoS_2 are visible (see open square in Figure 1f). Figure 1f shows a Raman map of the intensities of the characteristic Raman peaks of the 2D materials in use. Green represents the intensity of the hBN peak, purple depicts the G-peak intensity of the FLG, blue shows the intensity of the A_{1g} mode of the MoS_2. The dark areas are the gold shadow masks, which define the constriction in the underlying MoS_2 layer. Figure 1h shows a scanning electron microscopy image (SEM) of a typical device. The boundaries of the individual flakes are indicated by the dashed colored lines, where we use the same color code as in Figure 1e. Figure 1i shows an SEM image of a typical shadow mask structure with a width of 250 nm and a length of 175 nm.

We start by discussing charge transport in a few-layer MoS_2 Hall bar structure and explore the method of photodoping before discussing transport through the MoS_2 constrictions. The Hall bar device was fabricated the same way as described above. In Figure 2a we show the current I flowing through the Hall bar (see inset of Figure 2a), which is measured in standard four-terminal geometry in longitudinal configuration as function of the applied gate voltage V_g for temperatures ranging between 300 K to 5 K at a constant bias of V_b = 100 mV. Prior to photodoping (PD), the overall current strongly decreases with decreasing temperature and falls below our detection limit for temperatures less than 10 K (see corresponding green curve taken at 2 K in the inset of Figure 2b). The strong decrease of current at low temperatures is due to (i) a strong increase of the MoS_2 resistance and partially (ii) to an increase of the contact resistance (see supplementary materials, Figures S1a and S1b). The increase in resistivity of the MoS_2 is most likely due to localization effects. At higher temperatures, we observe a gate dependent insulator-to-metal transition seen by the onset of the current flow in Figure 2a, which continuously shifts to smaller gate voltages with increasing temperature. Similar observations of a charge carrier density dependent insulator-to-metal transition in MoS_2 have been recently reported.[32–34] Metallic conductance at low temperatures can be observed for high charge carrier densities around $n \approx 10^{13}$ cm^{-2}. In order to adjust the charge carrier density in our devices we make use of the recently reported photodoping mechanism across a hBN-to-graphene interface.[20,21,35] Nitrogen vacancies and/or carbon impurities in the hBN crystal can be optically activated and act as a charge reservoir in gated graphene. By illuminating our hBN/MoS_2/hBN Hall bar using a high energy light emitting diode (LED) with a center wavelength of 470 nm, these hBN defect states get optically excited. By applying a gate voltage, the activated charges are transferred into the MoS_2 layer leaving behind oppositely charged states in the hBN layer. The charge transfer continues until the applied (back gate induced) electric field gets fully screened by the charged hBN layer. When turning off the LED, the charges become trapped in the hBN resulting in a constant carrier doping of the illuminated area of MoS_2. In agreement with earlier work on similar photodoping of graphene,[21] we observe that the doping is stable over the entire measurement period (up to several weeks) in the temperature range between 2 K and 250 K. Figure 2b shows a series of gate characteristics of the

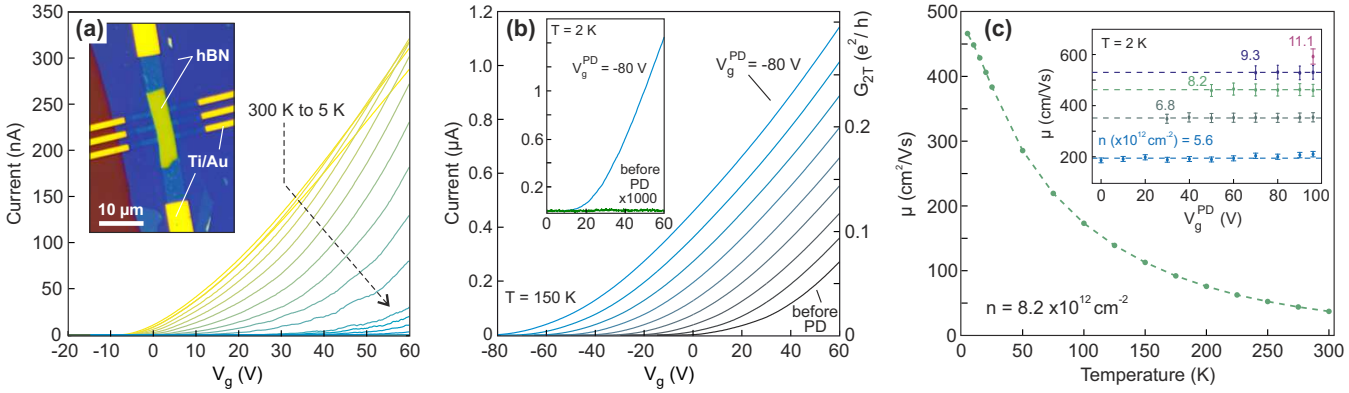

Figure 2. (a) Current through a Hall bar device as function of back gate voltage for temperatures ranging from 300 K to 5 K in steps of 25 K between 300 K and 25 K as well as steps of 5 K between 25 K and 5 K. Inset: optical microscope image of the Hall bar fabricated from a hBN/MoS_2/hBN/FLG van-der-Waals heterostructure. (b) Current as function of the gate voltage in a Hall bar for several consecutive photodoping steps of $V_g^{PD} = -10$ V. (c) Charge carrier mobility of the Hall bar as function of temperature, showing increased carrier mobility at low temperatures after photodoping at 150 K. Inset: Charge carrier mobility as function of the photodoping gate voltage for different charge carrier densities, indicating that photodoping does not influence the charge carrier mobility of the device.

Hall bar at 150 K before and after photodoping. The device was illuminated for 10 minutes at constant gate voltages varying between $V_g^{PD} = -10$ V and $V_g^{PD} = -80$ V in steps of $\Delta V_g = -10$ V. The gate characteristics show a respective overall increase in current, which corresponds well to shifts of $\Delta V_g = -10$ V in gate voltage. At the same time the gate characteristics remain identical in slope and shape indicating a constant charge carrier mobility and a homogeneous and efficient doping process throughout the entire device. After illuminating the Hall bar at $V_g^{PD} = -80$ V, the device shows metallic behavior, i.e. it remains well conductive at 2 K when applying moderate gate voltages (see inset of Figure 2b and supplementary materials Figure S2). Charge carrier mobilities extracted from Hall measurements on a typical device show values on the order of μ = 600 cm^2/(Vs) at low temperatures (2 K), which decreases to a value of around 45 cm^2/(Vs) at room temperature most likely due to electron-phonon scattering[32] (see Figure 2c). In the inset of Figure 2c, the charge carrier mobility at 2 K is plotted for different photodoping steps. For each photodoping step the device is warmed up to 150 K (as the LED is freezing out at low temperatures), the photodoping is performed and the device is cooled down again to 2 K to extract the low temperature mobility. The different colors represent different charge carrier densities. Similar to remote doping in 2DEGs,[36] the mobility of the device is not affected by the process of photodoping, as the charge that is introduced in the hBN flake is spatially separated from the MoS_2 (see colored dashed lines in the inset of Figure 2c). In order to underline the high electronic quality of the heterostructures, we also measure the quantum Hall effect in a MoS_2 Hall bar,[26] where we extract quantum mobilities on the order of 2,000 cm^2/(Vs) (see supplementary material Figure S3).

Next we discuss constriction devices. For observing size-quantization effects, including quantized conductance, the Fermi wavelength of the carriers has to be on the order of the device size, e.g. the width of the constriction. For reasonable carrier densities this requires devices with feature sizes on the order of 100 nm (or below). In order to harness photodoping for such small device feature sizes, we employ a shadow masking technique using non-transparent metal structures. Notably, this approach is in contrast to previous work, where some of us demonstrated photodoping with micron-scale spatial resolution using a confocal laser set-up.[21] The metallic shadow masks, predefined by electron beam lithography, allow to define long-lasting doping profiles in arbitrary geometries (see e.g. Figures 1g-1i). Using this shadow masking technique, we

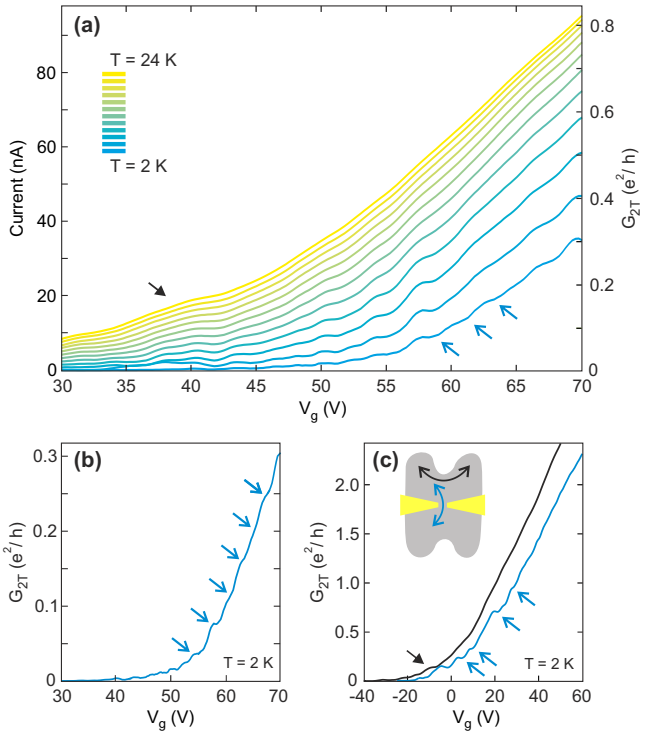

Figure 3. (a) Current through the constriction as function of gate voltage for different temperatures in steps of 2 K. Step-like features in the current are observed at low temperatures and get smoothed out with increasing temperature. The features vanish around 15 K. (b) Two-terminal conductance through the constriction at 2 K, showing kinks in the conductance (see blue arrows). (c) Current alongside (black trace) and through a four-terminal constriction (blue trace) as function of gate voltage after photodoping. The conductance trace alongside the constriction are smooth, whereas only the trace through the constriction exhibits step-like features in the current. Inset: schematic of the current flow corresponding to the different conductance traces.

illuminate only the source and drain contact areas (leads) and the constriction, while everything covered by metal is unaffected by the photodoping process. As the MoS_2 is non-conductive at 2 K prior to the photodoping no depletion is necessary to form a constriction between the metallic shadow masks. In contrast to conventional constrictions in 2DEGs, we neither have to etch our sample nor have to use electrostatic gates to define the structure as free car-

riers are only available in the regions, where the sample has been photodoped.

Figure 3a shows the two-terminal conductance through a 275 nm wide constriction at constant bias of V_b = 3 mV for temperatures ranging from 2 K to 24 K (after photodoping the device at 50 K and $V_g^{PD} = -60$ V). The conductance trace at 2 K shows step-like features suggesting size quantization effects in the constriction (see Figure 3b). A very similar behavior is observed for all four measured constriction devices (see supplementary material).

The step-like features in the conductance traces start to smear out with increasing temperature and remain visible up to 15 K (Figure 2a). The smearing may come from temperature broadening as one would expect that the conductance steps are washed out at a temperature $T \approx \Delta/k_B\pi$ with Δ the mode spacing. As we will see later $\Delta = 2-4$ meV for a similar device, which corresponds to $T = 7-15$ K.

In order to verify that the conductance steps originate from the constriction, we perform two-terminal measurements in different contact configurations on a separate multi-terminal device (see Figure 3c) with a constriction width of 250 nm. The black trace in Figure 3c shows the conductance between two contacts on one lead, i.e. on one side of the constriction of a four-terminal device, (see the black arrow in the inset of Figure 3c). The measurements were performed at 2 K after photodoping the device at $V_g^{PD} = -60$ V and 50 K. The trace shows a smooth and monotonic increase of the conductance with the applied gate voltage except for a feature close to the onset of the conductance at around $V_g = -5$ V and is similar in shape to the traces obtained from several Hall bar devices. In contrast, the conductance through the constriction (blue trace in Figure 3c) shows the same step-like features as they were observed for the two-terminal device.

The total resistance from the two-terminal data shown in Figure 3 heavily depends on the particular device and ranges between 10 and 100 kΩ and is thus significantly larger than the conductance quantum, as the contact resistances heavily contributes to the overall resistance. A subtraction of this parasitic resistances proves problematic as both are strongly gate voltage and bias dependent. In order to reduce the influence of these additional device resistances on the measurement, we perform four-terminal measurements on the multi-terminal device (see inset of Figure 4a). It is important to point out that this four-terminal measurement allows to extract an effective two-terminal conductance as the voltage is probed roughly 4 μm away from the constriction. This length is significantly larger than the elastic mean free path in the MoS_2. Figure 4a shows the four-terminal conductance as function of the applied gate voltage at 2 K. The conductance ranges from 0 to 10 e^2/h and shows step-like features with a step height close to e^2/h without any correction for an additional serial resistance. Notably, the feature near the onset of the conduction, which is seen in the conductance alongside the constriction is again visible at around V_g = 0 V (compare with the black arrow Figure 3c). In Figure 4b, we present the derivative of the conductance trace shown in Figure 4a with respect to gate voltage. The transconductance shows clear dips corresponding to the steps in the conductance. To extract an energy scale for these step-like features, we perform finite bias spectroscopy measurements at 2 K (see Figure 4c). Here, the bias axis corresponds to the measured bias at the voltage probes in the four-terminal configuration. The data shows diamonds at the positions of the steps, as one would expect for quantized conductance steps. The data is rather noisy for V_g up to 30 V which might originate from potential disorder. Above this value, we observe diamonds whose energy extend Δ_n is decreasing with increasing gate voltage.

For discussing these data and in particular for estimating an effective constriction width from the extracted energy scale, we follow a simple model assuming an electron in a potential well with the effective mass m^* close to the one of single-layer MoS_2.[37,38] The first observation is that the height of the conductance steps is given by e^2/h indicating a broken Kramers' and valley degeneracy even at zero magnetic field. Similar conductance steps of e^2/h have been observed in 1D wires, where interaction effects are more prominent.[39–41] In the present situation, we could speculate that the broken time-reversal symmetry arises due to localized spins trapped at impurity sites due to the potential disorder or at molybdenum antisites.[42]

In the model, the energy extend Δ_n of the n-th conductance step is associated with the mode spacing. As the height decreases with n, the transverse confinement is rather smooth (in fact smoother than parabolic as the latter leads to a constant energy spacing). We fit the data to a model of the form $\Delta_n = (2V_0/s^2)(s-n)$ that is derived for a Pöschel-Teller potential well in the limit $s \gg 1$.[43] A schematic of the potential can be seen in Figure 5a. Fitting a straight line (see Figure 5b), we obtain the depth $V_0 \approx 50$ meV of the potential and the number of bound states $s \approx 19$ (that corresponds to 19 confined modes). These values are connected to the width w at half maximum and the mass m of the electron via $2V_0/s^2 = 4\hbar^2/m^*w^2 \approx 0.27$ meV. This value can be now used to obtain an estimate for either w or m^* given the knowledge of the other.

We first assume a value $m^* \approx 0.4\ m_e$ for the effective mass of a single-layer MoS_2 as predicted by tight-binding models (see Refs.

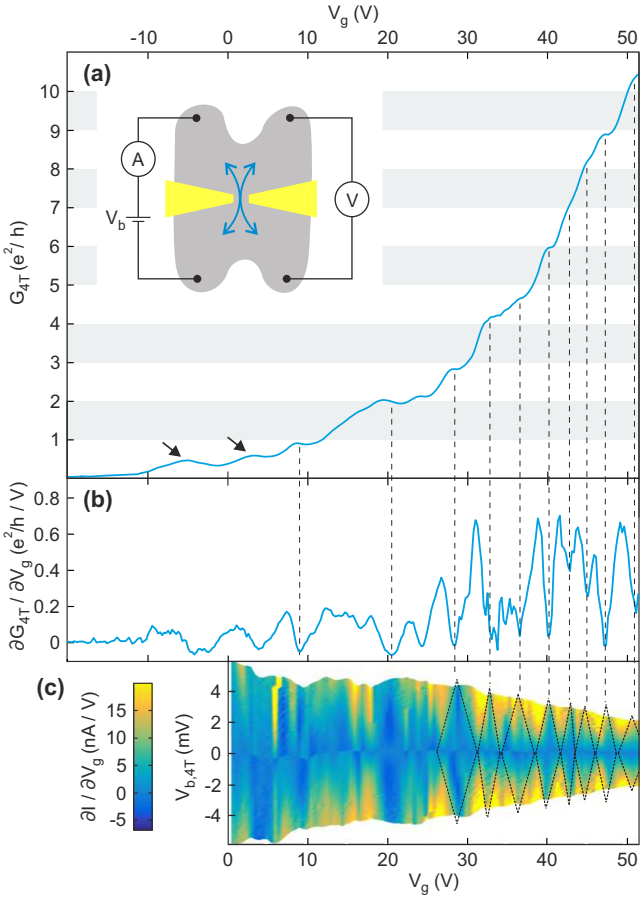

Figure 4. (a) Four-terminal conductance through the constriction as function of the applied gate voltage. Equidistant steps appear at multiples of e^2/h. (b) Derivative with respect to the applied gate voltage of the trace shown in (a), showing dips that correspond to the steps in (a). (c) Bias spectroscopy measurement showing diamonds at the positions of the steps, indicated by the black dashed lines.

37,38). If we assume that the Kramers' and valley degeneracy is broken on a scale $\simeq 20\,\mathrm{meV}$ such that all the modes in Figure 4 correspond to the same valley and spin index, we arrive at a value $w \approx 55\,\mathrm{nm}$. In the opposite extreme, we consider the case, where the Kramers' and valley-splitting is in the order of $2-5\,\mathrm{meV}$ such that the 4 symmetry broken modes succeed. In this case only every 4-th step corresponds to a higher mode in the confining potential thus V_0/s^2 is effectively a factor 4 larger and we obtain $w \approx 25\,\mathrm{nm}$. Note that the two estimates highlight the extreme cases and that the value of neither the Kramers' nor the valley-splitting can be smaller than a few meV as otherwise, we would observe steps of height $2e^2/h$.

We compare the scale ($25-55\,\mathrm{nm}$) with numerical simulations[44] of the (lateral) light intensity profile responsible for forming the constriction during photodoping. Figure 5a shows the simulated intensity distribution in the constriction region defined by a 250 nm spaced shadow mask. The simulation indicates that the light intensity underneath the shadow mask is suppressed, with a lateral extend of the intensity profile (at full-width-at-half-maximum) of 220 nm (see arrows in Figure 5d). We consider this value as an upper limit as we do not know (i) the intensity at which photodoping becomes efficient and (ii) to which extend electrostatic effects from the metallic shadow mask may affect the potential landscape in the constriction region. We believe that the factor 4 difference between the estimate above and the value as given by the simulation can be very well attributed to the effects (i) and/or (ii).

As an alternative explanation of the observed mode spacing, we investigate the possibility that the effective mass in few-layer MoS_2 is different from the one quoted above. In particular in few-layer MoS_2, the conduction band edge shifts from the K-point to the Q-point,[45] which may result in a slightly different effective mass. To investigate this possibility, we assume that $w = 220\,\mathrm{nm}$ and calculate the value of the effective mass m^* that corresponds to the extracted value of $2V_0^2/s^2$. With this procedure, we obtain the estimate $m^* \approx 0.07 m_e$ which is almost an order of magnitude smaller than the literature value such that we have come to the conclusion that a smaller effective mass cannot be the sole explanation of the observed mode spacing but rather the effective constriction is smaller than the lithographically defined geometry. All these findings motivates more detailed studies, which go beyond the scope of this work. Here, we highlight an interesting and promising approach to fabricate doping profiles in MoS_2 devices on length scales of tenth to hundreds of nanometer allowing to study quantum phenomena in this and related TMDC materials.

In summary, we present a technique to fabricate mesoscopic devices based on MoS_2 encapsulated by hBN using an entirely dry transfer process, contacting the MoS_2 using few-layer graphene and adjusting the charge carrier concentration using photodoping. By transferring only a single FLG flake to fabricate a large number of contacts to the MoS_2, we reduced the complexity of the required van-der-Waals heterostructure significantly. Similar to remote doping in 2DEGs, we are able to adjust the doping level in MoS_2, while preserving a "high" charge carrier mobility, resulting in metallic transport at low temperatures. By using metal shadow masks combined with photodoping, we demonstrate a way to produce complex doping profiles on a scale close to the diffraction limit, allowing to observe size quantization effects in MoS_2. In low temperature transport measurements, we reproducibly observe signatures of quantized conductance in MoS_2 constrictions. Even though gaining precise control over the exact confinement potential proves still to be difficult, our simulations suggest that the shadow masking technique can prove useful to generate smooth and long-lasting doping profiles in van-der-Waals heterostructures. This technique could pave the way towards the fabrication of other mesoscopic devices in TMDCs, such as for example Aharonov-Bohm rings or antidot lattices, which are difficult to realize using electrostatic gating.

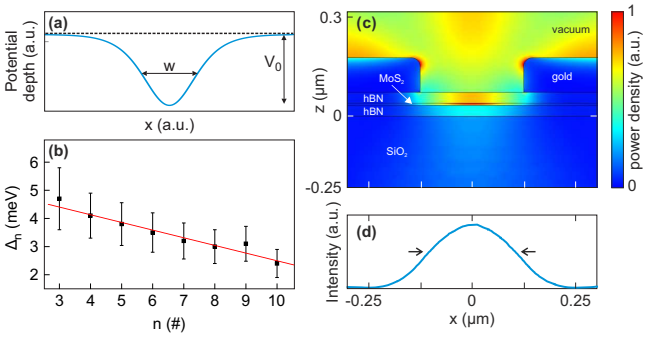

Figure 5. (a) A Pöschel-Teller potential well of the form $V \propto 1/\cosh^2$ with the depth of the potential V_0 and the full width at half maximum w. (b) Extracted energy extend Δ_n of the n-th diamond in Figure 4c. A straight line is fitted to the data between $n = 3$ and 10 yielding $\Delta_n = (-0.27 \pm 0.12)\,\mathrm{meV} \cdot n + (5.22 \pm 0.96)\,\mathrm{meV}$. (c) Simulation of the intensity distribution in the constriction region defined by a shadow mask assuming vertical illumination of the sample. (d) Intensity profile of a cross-section through the bottom hBN for 250 nm spaced shadow masks. The full-width-at-half-maximum yields a width of 220 nm.

Acknowledgement

The authors thank F. Haupt for fruitful discussions and S. Kuhlen for help with the figures. Support by the Helmholtz-Nanoelectronic-Facility (HNF), the DFG (SPP-1459), the ERC (GA-Nr. 280140), and the EU project Graphene Flagship (contract no. NECT-ICT-696656) are gratefully acknowledged. Growth of hexagonal boron nitride crystals was supported by the Elemental Strategy Initiative conducted by the MEXT, Japan and JSPS KAKENHI Grant Numbers JP26248061, JP15K21722 and JP25106006.

References

(1) K. S. Novoselov, A. Mishchenko, A. Carvalho, A. H. Castro Neto, 2D materials and van der Waals heterostructures. Science **2016**, 353, 6298.
(2) A. K. Geim and I. V. Grigorieva, Van der Waals heterostructures. Nature **2013**, 499, 419-425.
(3) B. Radisavljevic, A.Radenovic, J.Brivio, V. Giacometti and A. Kis, Single-layer MoS_2 transistors. Nat. Nanotechnol. **2011**, 6 , 147-150.
(4) B. W. H. Baugher, H. O. H. Churchill, Y. Yang and P. Jarillo-Herrero, Intrinsic Electronic Transport Properties of High-Quality Monolayer and Bilayer MoS2. Nano Lett. **2013**, 13, 4212-4216.
(5) S. Russo, J. B. Oostinga, D. Wehenkel, H. B. Heersche, S.S. Sobhani, L. M. Vandersypen, A. F. Morpurgo, Observation of Aharonov-Bohm conductance oscillations in a graphene ring. Phys. Rev. B **2008**, 77, 085413.
(6) B. Terrés, L. A. Chizhova, F. Libisch, J. Peiro, D. Jörger, S. Engels, A. Girschik, K. Watanabe, T. Taniguchi, S. V. Rotkin, J. Burgdörfer and C. Stampfer, Size quantization of Dirac fermions in graphene constrictions. Nat. Commun. **2016**, 7, 11528.
(7) J. M. Elzerman, R. Hanson, L.W. Van Beveren, B. Witkamp, L.M.K. Vandersypen and L.P. Kouwenhoven, Single-shot read-out of an individual electron spin in a quantum dot. Nature **2004**, 430, 431-435.
(8) B. J. van Wees, H. van Houten, C. W. J. Beenakker, J. G. Williamson, L. P. Kouwenhoven, D. van der Marel and C. T. Foxon, Quantized conductance of point contacts in a two dimensional electron gas. Phys. Rev. Lett. **1988**, 60, 848.
(9) I. van Weperen, S. R. Plissard, E. P. A. M. Bakkers, S. M. Frolov, and L. P. Kouwenhoven, Quantized conductance in an InSb nanowire. Nano Lett. **2013**, 13, 387-391.
(10) A. T. Johnson, L. P. Kouwenhoven, W. De Jong, N. C. Van der Vaart, C. J. P. M. Harmans, and C. T. Foxon, Zero-dimensional states and single electron charging in quantum dots. Phys. Rev. Lett. **1992**, 69, 1592-1596.
(11) A. Rycerz, J. Tworzydlo and C. W. J. Beenakker, Valley filter and valley valve in graphene. Nat. Phys. **2007**, 3, 172-175.
(12) N. Tombros, A. Veligura, J. Junesch, M. H. D. Guimaraes, I. J. Vera Marun, H. T. Jonkman and B. J. van Wees, Quantized conductance of a suspended graphene nanoconstriction. Nat. Phys. **2011**, 7, 697-700.
(13) D. Bischoff, F. Libisch, J. Burgdörfer, T. Ihn, and K. Ensslin, Characterizing wave functions in graphene nanodevices: Electronic transport through ultrashort graphene constrictions on a boron nitride substrate. Phys. Rev. B **2014**, 90, 115405.
(14) A. M. Goossens, S. C. M. Driessen, T. A. Baart, K. Watanabe, T. Taniguchi, and L. M. K. Vandersypen, Gate-Defined Confinement in Bilayer Graphene-Hexagonal Boron Nitride Hybrid Devices. Nano Lett. **2012**, 12, 4656-4660.

(15) M. T. Allen, J. Martin, and A. Yacoby, Gate-defined quantum confinement in suspended bilayer graphene. Nat. Commun. **2012**, 3, 934.
(16) X.-X. Song, D. Liu, V. Mosallanejad, J. You, T.-Y. Han, D.-T. Chen, H.-O. Li, G. Cao, M. Xiao, G.-C. Guo and G.-P. Guo, A gate defined quantum dot on the two-dimensional transition metal dichalcogenide semiconductor WSe_2. Nanoscale **2015**, 7, 16867-16873.
(17) K. Wang, T. Taniguchi, K. Watanabe and P. Kim, Engineering Quantum Confinement in Semiconducting van der Waals Heterostructure. arXiv:1610.02929, (2016).
(18) D. Goldhaber-Gordon, Hadas Shtrikman, D. Mahalu, D. Abusch-Magder, U. Meirav and M. A. Kastner, Kondo effect in a single-electron transistor. Nature **1998**, 391, 156.
(19) J. R. Petta, A. C. Johnson, J. M. Taylor, E. A. Laird, A. Yacoby, M. D. Lukin, C. M. Marcus, M. P. Hanson and A. C. Gossard Coherent manipulation of coupled electron spins in semiconductor quantum dots. Science **2005**, 309, 2180.
(20) L. Ju, J. Velasco Jr., E. Huang, S. Kahn, C. Nosiglia, H.-Z. Tsai, W. Yang, T. Taniguchi, K. Watanabe, Y. Zhang, G. Zhang, M. Crommie, A. Zettl and F. Wang, Photoinduced Doping in Heterostructures of Graphene and Boron Nitride. Nat. Nanotechnol. **2014**, 9, 348-352.
(21) C. Neumann, L. Rizzi, S. Reichardt, B. Terres, T. Khodkov, K. Watanabe, T. Taniguchi, B. Beschoten, and C. Stampfer, Spatial control of laser-induced doping profiles in graphene on hexagonal boron nitride. ACS Appl. Mater. Interfaces **2016**, 8, 9377-9383.
(22) L. Wang, I. Meric, P. Y. Huang, Q. Gao, Y. Gao, H. Tran, T. Taniguchi, K. Watanabe, L. M. Campos, D. A. Muller, J. Guo, P. Kim, J. Hone, K. L. Shepard, and C. R. Dean, One-Dimensional Electrical Contact to a Two-Dimensional Material. Science **2013**, 342, 614-617.
(23) L. Banszerus, M. Schmitz, S. Engels, J. Dauber, M. Oellers, F. Haupt, K. Watanabe, T. Taniguchi, B. Beschoten and C. Stampfer, Ultrahigh-mobility graphene devices from chemical vapor deposition on reusable copper. âĂŐSci. Adv **2015**, 1, e1500222.
(24) L. Yu, Y.-H. Lee, X. Ling, E. J. G. Santos, Y. C. Shin, Y. Lin, M. Dubey, E. Kaxiras, J. Kong, H. Wang, and T. Palacios, Graphene/MoS_2 hybrid technology for large-scale two-dimensional electronics. Nano Lett. **2014**, 14, 3055-3063.
(25) T. Roy, M. Tosun, J. S. Kang, A. B. Sachid, S. B. Desai, M. Hettick, C. C. Hu, and A. Javey, Field-effect transistors built from all two-dimensional material components. ACS Nano **2014**, 8, 6256-6264.
(26) X. Cui, G.-H. Lee, Y. D. Kim, G. Arefe, P. Y. Huang, C.-H. Lee, D. A. Chenet, X. Zhang, L. Wang, F. Ye, F. Pizzocchero, B. S. Jessen, K. Watanabe, T. Taniguchi, D. A. Muller, T. Low, P. Kim and J. Hone, Multi-terminal transport measurements of Mo using a van der Waals heterostructure device platform. Nat. Nanotechnol. **2015**, 10, 534-540.
(27) R. Kappera, D. Voiry, S. E. Yalcin,B. Branch, G. Gupta, A. D. Mohite and M. Chhowalla, Phase-engineered low-resistance contacts for ultrathin MoS_2 transistors. Nat. Mater. **2014**, 13, 1128-1134.
(28) L.M. Malard, M.A. Pimenta, G. Dresselhaus, M.S. Dresselhaus, Raman spectroscopy in graphene. Phys. Rep. **2009**, 473, 51-87.
(29) R. Gorbachev, I. Riaz, R. R. Nair, R. J. L. Britnell, B. D. Belle, E. W. Hill, K. S. Novoselov, A. K. Geim, P. Blake, Hunting for Monolayer Boron Nitride: Optical and Raman Signatures, Small **2011**, 7, 465-468.
(30) P. Tonndorf, R. Schmidt, P. Böttger, X. Zhang, J. Börner, A. Liebig, M. Albrecht, C. Kloc, O. Gordan, D. R. T. Zahn, S. Michaelis de Vasconcellos, and R. Bratschitsch, Photoluminescence emission and Raman response of monolayer MoS_2, $MoSe_2$, and WSe_2. Opt. Express **2013**, 21, 4908-4916.
(31) H. Sahin, S. Tongay, S. Horzum, W. Fan, J. Zhou, J. Li, J. Wu, and F. M. Peeters, Anomalous Raman spectra and thickness-dependent electronic properties of WSe_2. Phys. Rev. B **2013**, 87, 165409.
(32) B. Radisavljevic and A. Kis, Mobility engineering and a metal-insulator transition in monolayer MoS_2. Nat. Mater. **2013**, 12, 815-820.
(33) B. W. H. Baugher, H. O. H. Churchill, Y. Yang, and P. Jarillo-Herrero, Intrinsic Electronic Transport Properties of High-Quality Monolayer and Bilayer MoS_2. Nano Lett. **2013**, 13, 4212-4216.
(34) H. Schmitt, S. Wang, L. Chu, M. Toh, R. Kumar, W. Zhao, A. H. Castro Neto, J.Martin, S. Adam, B. Özyilmaz, and G. Eda, Transport Properties of Monolayer MoS_2 Grown by Chemical Vapor Deposition. Nano Lett. **2014**, 14, 1909-1913.
(35) D. Wong, J. Velasco Jr, L. Ju, J. Lee, S. Kahn, H.-Z. Tsai, C. Germany, T. Taniguchi, K. Watanabe, A. Zettl, F. Wang and M. F. Crommie, Characterization and manipulation of individual defects in insulating hexagonal boron nitride using scanning tunnelling microscopy. Nat. Nanotechnol. **2015**, 10, 949-953.
(36) R. Dingle, H. L. Störmer, A. C. Gossard, and W. Wiegmann, Electron mobilities in modulation-doped semiconductor heterojunction superlattices. Appl. Phys. Lett. **1978**, 33, 665.
(37) H. Rostami, A. G. Moghaddam, and R. Asgari, Effective lattice Hamiltonian for monolayer MoS_2: Tailoring electronic structure with perpendicular electric and magnetic fields. Phys. Rev. B **88**, 085440 (2013).
(38) A. Kormanyos, V. Zolyomi, N. D. Drummond, and G. Burkard, Spin-Orbit Coupling, Quantum Dots, and Qubits in Monolayer Transition Metal Dichalcogenides. Phys. Rev. X **4**, 011034, (2014).
(39) M. J. Biercuk, N. Mason, J. Martin, A. Yacoby, and C. M. Marcus, Anomalous Conductance Quantization in Carbon Nanotubes. Phys. Rev. Lett. **2005**, 94, 026801.
(40) J. Moser, T. Zibold, D. Schuh, M. Bichler, F. Ertl, G. Abstreiter, M. Grayson, S. Roddaro, and V. Pellegrini, Aluminum arsenide cleaved-edge overgrown quantum wires. Appl. Phys. Lett. **2005**, 87, 052101.
(41) G. Scappucci, L. Di Gaspare, E. Giovine, A. Notargiacomo, R. Leoni, and F. Evangelisti, Conductance quantization in etched Si/SiGe quantum point contacts. Phys. Rev. B **2006**, 74, 035321.
(42) J. Hong, Z. Hu, M. Probert, K. Li, D. Lv, X. Yang, L. Gu, N. Mao, Q. Feng, L. Xie, J. Zhang, D. Wu, Z. Zhang, C. Jin, W. Ji, X. Zhang, J. Yuan, and Z. Zhang, Exploring atomic defects in molybdenum disulphide monolayers. Nature Comm. **6**, 6293 (2015).
(43) L. D. Landau and E. M. Lifshitz, Quantum Mechanics, prob. 5 in §23 of vol. 3 of Course of Theoretical Physics (Pergamon Press, London, 1958).
(44) The simulations were performed using COMSOL Multiphysics and assumes vertical illumination of the sample.
(45) E. Cappelluti, R. Roldan, J. A. Silva-Guillen, P. Ordejon and F. Guinea. Tight-binding model and direct-gap/indirect-gap transition in single-layer and multilayer MoS_2. Phys. Rev. B **2013**, 88, 075409.